Article:
Thomas, E, Simolka, J, DeLuca, M et al. (6 more authors) (2017) Experimental setup for the laboratory investigation of micrometeoroid ablation using a dust accelerator. Review of Scientific Instruments, 88 (3). 034501. ISSN 0034-6748

https://doi.org/10.1063/1.4977832

Last Edit: 28 March 2017 15:47

Experimental setup for the laboratory investigation of micrometeoroid ablation using a dust accelerator

Evan Thomas,[1, 2, a)] Jonas Simolka,[3] Michael DeLuca,[4, 1, 5] Mihály Horányi,[1, 2, 5] Diego Janches,[6] Robert A. Marshall,[7, 4] Tobin Munsat,[1, 2] John M.C. Plane,[8] and Zoltan Sternovsky[1, 5, 4, b)]

[1)] *IMPACT, University of Colorado, Boulder, CO 80303, USA*

[2)] *Physics Department, University of Colorado, Boulder, CO 80309, USA*

[3)] *Universität Stuttgart, Institut für Raumfahrtsysteme, Pfaffenwaldring 29, 70569 Stuttgart, Germany*

[4)] *Aerospace Engineering Sciences, University of Colorado, Boulder, CO 80309, USA*

[5)] *Laboratory for Atmospheric and Space Physics, University of Colorado, Boulder, CO 80303, USA*

[6)] *Space Weather Laboratory, NASA Goddard Space Flight Center, Greenbelt, MD 20771, USA*

[7)] *Colorado Center for Astrodynamics Research (CCAR), University of Colorado, Boulder, CO 80309, USA*

[8)] *School of Chemistry, University of Leeds, Leeds, UK*

(Dated: 28 March 2017)

A facility has been developed to simulate the ablation of micrometeoroids in laboratory conditions. An electrostatic dust accelerator is used to generate iron particles with velocities of 10-70 km/s. The particles are then introduced into a chamber pressurized with a target gas, where the pressure is adjustable between 0.01-0.5 Torr, and the particle partially or completely ablates over a short distance. An array of biased electrodes above and below the ablation path is used to collect the generated ions/electrons with spatial resolution of 2.6 cm along the ablating particles' path, thus allowing the study of the spatiotemporal evolution of the process. For completely ablated particles, the total collected charge directly yields the ionization coefficient of a given dust material-target gas combination. The first results of this facility measured the ionization coefficient of iron atoms with N_2, air, CO_2, and He target gases for impact velocities > 20 km/s, and is reported by Thomas *et al.*[1]. The ablation chamber is also equipped with four optical ports that allow for the detection of the light emitted by the ablating particle. A multichannel PMT system is used to observe the ablation process with a spatial and temporal resolution of 0.64 cm and 90 ns. The preliminary results indicate that it is possible to calculate the velocity of the ablating particle from the optical observations, and in conjuction with the spatially-resolved charge measurements, allow for experimental validation of ablation models in future studies.

I. INRODUCTION

A new facility has been developed for the study of the meteor ablation process in laboratory conditions. The motivation for the research is the detailed understanding of the processes taking place during the ablation of micrometeoroids in the Earth's and other planetary atmospheres. The measurements are intended to validate existing ablation models and measure critical parameters used by the models. For example, the facility allows the direct measurement of the ionization coefficient, β, which is the probability of ionization of an ablated atom through collisions with the background gas. The enabling facility is the 3 MV dust accelerator at the University of Colorado, which provides micron and sub-micron sized particles with velocities in the relevant range, i.e. 10-70 km/s[2]. The ablation facility described in this work uses a differential pumping system to connect the high vacuum dust accelerator's beamline to a gas-filled chamber where complete or partial ablation takes place over a short distance. Charge collecting electrodes and photomultiplier tubes are used to detect the generated plasma of the ablation and the plasma light production. Preliminary tests confirm that the facility is sufficiently sensitive to detect the ablation process, even at the lower end of the velocity range of interest, and measure the velocity of the ablating particle from optical observations. It is demonstrated that these measurements will allow for experimental validation of commonly used ablation models in future studies.

Recently, Thomas *et al.*[1] reported the first scientific results from the ablation facility described in this article. That work measured the ionization coefficient of iron particles impacting N_2, air, CO_2, and He, and compared the new experimental values to a commonly used analytical theory[3] and past experimental work. The motivation for this article is to describe the ablation facility in more detail.

[a)] evan.w.thomas@colorado.edu

[b)] Zoltan.Sternovsky@lasp.colorado.edu

A. Motivation and importance

The Earth's atmosphere is continually bombarded by Interplanetary Dust Particles (IDPs) with typical masses of 1-10 μg[4]. The main sources of IDPs are decaying cometary trails and fragments from the asteroid belt. As these particles ablate in the upper atmosphere, they produce neutral layers of metal atoms such as: iron (Fe), magnesium (Mg), calcium (Ca), potassium (K) and sodium (Na) that peak around 90 km[4]. These atomic metal layers in the Earth's upper atmosphere are responsible for a diverse range of aeronomical phenomena including the nucleation of noctilucent clouds, ocean fertilization with bio-available Fe, and effects on the stratospheric aerosol and O_3 chemistry[4]. Furthermore, IDP measurements at Earth provide constraints on inner solar system dust/meteor models, which provide insight into the evolution and planetary formation processes of solar systems[5,6]. Therefore, the total micrometeoroid mass input into the atmosphere is a quantity of significant interest.

Existing estimates of the mass input range from 5 to 100 t/d (tons per day), depending on the method of measurement, ranging from meteor radar observations to ice core measurements in Greenland[7]. The factor of 20 uncertainty in the incoming meteoric mass is in part due to the wide range of particle masses/sizes and the lack of a single technique that provides measurement of the flux over the entire mass range. The bulk of the incoming material is from particles in the range of $10^{-10} - 1$ g with a peak at around 10^{-5} g ($\sim$100 μm in radius[8]). The wide range of incoming velocities, 11-72 km/s[9], further complicates the situation as some measurement methods for inferring flux depend strongly on both the mass and the velocity of the particles.

Radar measurements play a critical role in the observation of the incoming extraterrestrial particles, as this technique is (1) sensitive to the size range where most of the mass input occurs[4]; and (2) the existing radar facilities provide continuous observation. Particles entering the atmosphere with velocities >11 km/s produce luminous trails of ionized gas that allow for the detection and characterization of individual meteors[10–13]. Radar observations of meteors are sensitive to particles with masses between $10^{-9} - 10^{-3}$ g.

The interpretation of meteor observation using radar techniques is subject to a number of biases, as the ablation and ionization are functions of the particles' mass, density and incoming velocity and angle. Such biases also depend on the scattering mechanisms being considered (e.g. head echo observations have different biases than specular trail observations[14]). The ionization coefficient, β, is a critical parameter in these measurements in that it relates the physical ablation of the meteor to the intensity of the radar return. However, there remain significant uncertainties in the β values for the various chemical components of micrometeoroids and atmospheric gases. Furthermore, the physical models describing the ablation process, including the differential ablation of the various chemical components, have not yet been fully validated in laboratory experiments. This introduces various biases in the radar measurements with velocity, size and composition[12,15].

Recently, Janches *et al.*[15] described the difficulty of reconciling meteor head echo observations using the Arecibo 430 MHz radar with the Zodiacal Dust Cloud (ZDC) model by Nesvorný *et al.*[5]. The ZDC model predicts that most of the IDP mass reaching the Earth are particles from Jupiter Family Comets (JFCs) in the 1-10 μg range with an average velocity of 14 km/s[16]; however, this population is missing from the radar measurements, which raises the question whether the lack of detection is due to their inexistence or an inability of the radars to detect them. Given these inconsistencies, it was suggested that lowering β by one or two orders of magnitude would bring the radar measurements into better agreement with the ZDC model. However, the first results of this facility (reported in Thomas *et al.*[1]) showed that β is most likely not a significant factor in the discrepancy.

The motivation of this facility is therefore to simulate the entire ablation process in a laboratory setting, because every one of the IDP influx measurement methods measures some outcome of this process (ionization, release of Na, Fe, etc.). A laboratory simulation of the ablation process allows for direct validation of ablation models which are critical to the interpreation of the various methods of measuring IDPs.

B. Previous laboratory ablation measurements

Much of the previous laboratory ablation research has focused on measuring particular ablation parameters, such as the ionization coefficient. There are two types of experimental methods for determining the ionization coefficient of meteors. In the first, high-velocity neutral metal atoms are introduced into a collision chamber filled with the target gas and the ionizing collision cross section is measured (where β is the ratio of the ionization cross section to the total cross section). Out of the materials relevant for meteoroid composition, this method has been applied only to alkali metals[17–19].

The second experimental method, which includes the facility described here, uses a dust accelerator that generates small particles with high velocities. The accelerated particles enter a pressurized chamber, where the partial or complete ablation occurs over a short distance. With the assumption that individual atoms sputter or evaporate off of the surface of the particle and collide with the background gas, the ionization coefficient can be directly measured by collecting the number of ion-electron pairs produced in the case of complete ablation (collisions/diffusion are considered in Section III A). The ionization coefficient is then simply the total number of ion-electron pairs divided by the total number of atoms in the particle. Slattery and Friichtenicht[20] measured β

for iron particles ablating in argon gas and air in the velocity range of 20 - 40 km/s. Friichtenicht, Slattery, and Hansen [21] extended the measurements for a wider range of background gases, including N_2 and O_2. Friichtenicht and Becker [22] used air as the target gas and dust particles made of Cu and LaB_6.

The current understanding of β and its variation with velocity is based on these experimental results, which are limited for non-alkali metals, with the exception of the recent β measurements by Thomas *et al.* [1]. Those results were used to provide experimental parameters for the commonly used Jones [3] analytical β model, and also demonstrated that the model effectively describes the velocity variation of β for iron particles impacting N_2 and air with atmospherically relevant speeds with the exception of high-speed impacts (> 70 km/s).

The ablation facility described here, as well as the recently developed Meteoric Ablation Simulator (MASI)[16], are the first laboratory experiments capable of measuring the ablation process and not limited to measuring particular ablation parameters. The MASI instrument simulates ablation after assuming a particular heating profile. In particular, it uses a heating filament to replicate the heating profile predicted from ablation models. However, the temperature profile must be calculated from meteor physics equations and assume values for parameters like the free molecular drag coefficient and the free molecular heat transfer coefficient[16].

C. Ablation in laboratory conditions

The experimental setup described here makes it possible to simulate the ablation process and benchmark ablation models against well-defined laboratory data and obtain important physical parameters. The typical size of micrometeoroids in Earth's atmosphere is 100 μm, and the ablation takes place over many kilometers. This process is simulated in the laboratory accelerator setup with both parameters scaled down significantly. The typical size of the particles used in the accelerator are $\sim$0.05 μm and the ablation chamber is 41 cm long, requiring higher pressures to achieve complete ablation. The relevant parameters, however, are similar in the two conditions. First, the ablation in both cases occurs in the free molecular regime, where the dust size ($\sim$0.05 μm) is much smaller than the mean free path between atomic or molecular collisions ($\sim$100 μm for the highest pressures). Second, based on the value of the Biot number being $Bi < 0.1$ up to high temperatures, Vondrak *et al.* [23] argued that typical (e.g. olivine) micrometeoroids will remain isothermal during the ablation process. For a spherical object, the Biot number is defined as $Bi = \frac{hR}{3k}$, where h is the heat transfer coefficient, R is the radius, and k is the thermal conductivity. Since the Biot number is proportional to the radius of the particle and inversely proportional to the thermal conductivity, the isothermal condition is valid for the smaller iron particles typically used in the laboratory experiments. Therefore, the basic physics of the ablation process, which are dependent on the assumption of the free molecular regime and the isothermal condition, are the same as the ablation of micrometeoroids in the atmosphere.

The composition of the meteors entering the atmosphere can be complex, which may lead to the interesting phenomena of differential ablation (see, for example, Janches *et al.* [12]). The volatile elements (Na, K, e.g.) are evaporated first at lower temperatures and higher altitudes, while more heating and higher temperatures are needed for the evaporation of the refractory elements. The differential ablation of Na, Fe, and Ca has already been observed using the MASI[16]. Iron dust is used in the initial measurements described in this article, which provides the benefit of direct comparison with earlier measurements and models. Measurements of dust particles with different compositions will be performed in future studies.

II. ABLATION FACILITY

A. Design overview

The high-velocity dust particles are generated using a 3MV electrostatic accelerator, which is described in detail by Shu *et al.* [2]. The particles, with an initial charge Q_D, are accelerated from a dust source mounted at the high voltage terminal. The particles travel down the beamline which is equipped with a set of image charge detectors. The amplitude and timing of the detector signals is measured by a field-programmable gate array (FPGA) particle selection unit[24], which provides the value of Q_D and the velocity v, and in turn allows for the mass calculation,

$$m = \frac{2Q_D U_A}{v^2}, \tag{1}$$

where U_A is the accelerating voltage. The accelerator provides a characteristic mass vs. velocity distribution of the accelerated particles, shown in Figure 1. For particles with relevant meteoric velocities (10-70 km/s), the particle radii range from 20-100 nm. One should also note that the accelerator is capable of providing particles with velocities > 70 km/s. These velocities correspond to the much rarer population of interstellar dust particles, which have velocities up to $\sim$ 70 km/s, or even larger[25].

The particle's path through the experimental setup at the end of the main beamline (see Figure 2 for a schematic) is as follows. Before entering the experimental setup, the particle moves through an image charge detector, which provides a velocity and mass measurement, as stated above. The particle then moves through a narrow tube (5 mm diamter) into the first stage of differential pumping, which is designed to separate the high

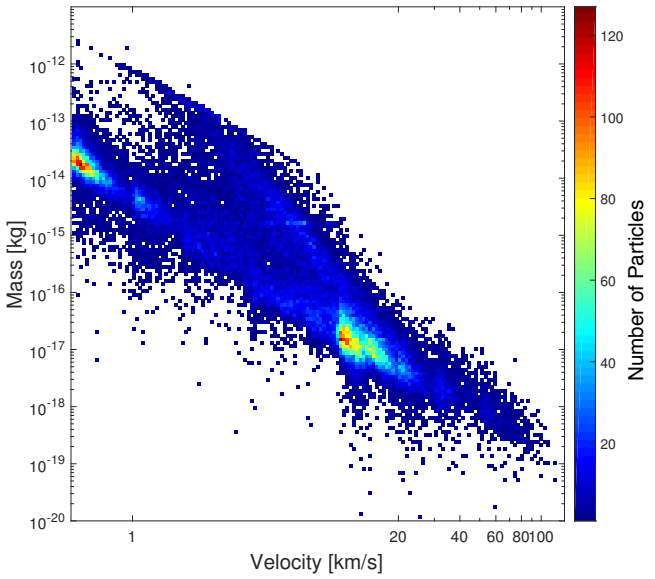

FIG. 1. A representative particle distribution from the accelerator. There is a large dynamic range of masses (8 orders of magnitude) and velocities (2 orders of magnitude) that the accelerator produces.

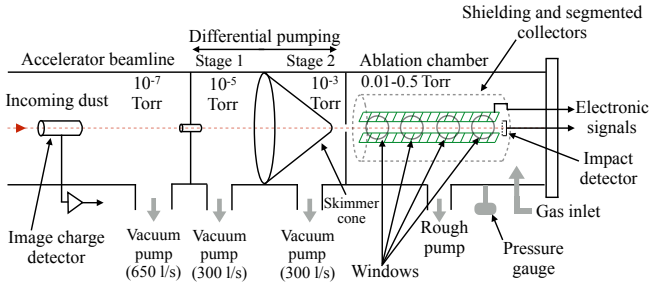

FIG. 2. Schematic of the experimental setup (side view). The particles are accelerated to > 10 km/s using the accelerator facility and the ablation chamber is mounted at the end of the beamline. A two stage differential pumping system separates the high vacuum beamline from the pressurized ablation chamber.

vacuum beamline (10^{-7} Torr) from the pressurized ablation chamber (0.01-0.5 Torr). Next, the particle moves through a skimmer cone that protrudes into the second stage of differential pumping before entering the ablation chamber through a 3 mm aperture. Inside the ablation chamber, the particle collides with the target gas and begins to heat, melt, and ablate (evaporate). The ablated dust atoms collide with molecules of the target gas and ionize with a certain probability given by β. This process generates a trail of plasma as the particle moves through the 41 cm ablation chamber.

The ablation chamber diagnostics allow for the observation of the ablation process in two ways: biased electrodes above and below the ablation path collect the generated plasma, and four windows evenly spaced along the ablation path allow for optical measurements. The electrodes are segmented, with each segment connected to a separate charge sensitive amplifier (CSA) in order to resolve the ionization as a function of distance. An impact detector (described in detail in Section II C) is placed at the end of the chamber to measure the impact charge generated by the remaining particle, if any. The amplitude of the impact charge signal provides the mass of the remaining particle.

B. Differential pumping system

A differential pumping system (shown in Figure 2) separates the high vacuum beamline from the pressurized ablation chamber. In order to observe all of the ablation physics, the differential pumping must have low enough pressures so that the dust particle's temperature does not increase significantly (< 100 K) before entering the ablation chamber. To achieve this, there are two stages of differential pumping, each 20 cm in length. The first stage (10^{-5} Torr) of the differential pumping is separated from the beamline (10^{-7} Torr) through a cylindrical tube 5 mm in diameter and 8 cm long, and is pumped by a 300 l/s turbomolecular pump with a dry scroll forepump. The second stage (10^{-3} Torr) contains a concentric skimmer cone with the larger end welded onto the chamber wall and is also pumped by a 300 l/s turbomolecular pump. The skimmer cone extends the effective length of the first stage by protruding into the second stage until the cone terminates 3 cm before the ablation chamber. Therefore, the particle is in the lower pressure environment of the first stage until just before entering the ablation chamber. Both the end of the cone and the entrance to the ablation chamber have adjustable apertures. The preliminary experiments were performed with 3 mm apertures for both the cone and the ablation chamber.

As stated previously, the goal of the differential pumping is to keep dust heating to < 100 K before entering the ablation chamber, and therefore the pressures in both stages were measured for the entire operating pressure range of the ablation chamber (0.01-0.5 Torr). In the case of the highest ablation chamber pressure (0.5 Torr), the pressure in the second differential pumping stage was measured to be 2 mTorr. Therefore, 2 mTorr was used as the pressure in an ablation simulation to ascertain if the differential pumping system succeeds in limiting dust heating to < 100 K. The simulation code used is a thermodynamic code described in Hood and Horányi[26] and Kalashnikova *et al.*[27]. The code assumes diffuse reflection of gas particles off of the dust surface and calculates drag and heating coefficients for the particle along its trajectory. It accounts for phase transitions and calculates the mass loss due to evaporation. For 2 mTorr, the particle's temperature increased by 5 K over 3 cm, which is the distance the particle travels from exiting the skimmer cone to entering the ablation chamber. For the

temperature to increase by 100 K, the particle would have to travel 50 cm, which is longer than both stages combined. Therefore, we concluded that the particles do not undergo significant heating before entering the ablation chamber.

C. Ablation chamber overview

The ablation chamber is first evacuated and then backfilled with the target gas using an Alicat MC-200SCCM mass flow controller. The pressure in the chamber is monitored using a Baratron 622C gauge for a gas-independent, absolute pressure measurement with a resolution of 0.1 mTorr. By adjusting the mass flow controller, the user is able to select the desired fate of the particle from modest heating to complete ablation. The approximate mean free path in the chamber is 0.1 - 5 mm for neutral-neutral and ion-neutral momentum exchange collisions.

The generated plasma from the ablation is collected on 16 segmented charge collection plates above and below the ablation path (see Figure 2). Each plate is connected to a charge sensitive amplifier (CSA) circuit which converts the collected charge to a measurable voltage. The top and bottom plates are separated by 3.6 cm, and each plate is 8 cm long (transverse to the beamline) and 2.6 cm wide (along the beamline axis). This gives a spatial resolution of 2.6 cm. One side of the plates is biased by +/- 90 V, creating an electric field oriented vertically in the chamber which separates the ions and electrons, so that each species is collected separately. The bias voltage is well below the Paschen breakdown voltage limit and creates an electric field which dominates over the initial kinetic energy of the ions/electrons after a few collisions with molecules of the background gas. Therefore, the ions/electrons are collected close to where they were generated. See section III A for a full discussion of this point.

If the particle does not fully ablate, whatever mass is left over will strike an impact detector at the end of the ablation chamber (see Figure 2) and generate a charge signal from which the remaining mass can be calculated. An impact detector is a common way of detecting dust particles through impact ionization (see, for example, Auer [28] and Collette *et al.* [29]). The impact detector consists of a tungsten coated charge collection plate (also connected to a CSA) with a biased high-throughput grid in front of it. The tungsten target is grounded, while the grid is biased at the same potential as the plates. When a particle impacts the tungsten target, ions and electrons are generated through impact ionization. Those ions and electrons are then separated by the electric field (generated by the biased grid) and collected on the tungsten target. The impact charge signal allows for the measurement of the remaining mass of the particle that did not ablate. This can be used simply as a way of noting whether the particle fully ablated, or it can be used quantitatively for comparisons to predictions from ablation models.

Four windows evenly spaced along the ablation path allow for optical measurements of the ablation process. The windows are 3.6 cm diameter quartz windows mounted on 7 cm flanges. The flanges allow for mounting photomultiplier tubes (PMTs) that can be used for light measurements. A full description of the PMT setup can be found in Section II E.

D. Charge collection CSA design

The design of the electronics for collecting the charge on the segmented electrodes is critical, as it sets the limit of sensitivity. Figure 3 shows the schematic of the CSA. The CSA circuit consists of three stages: a charge sensitive amplifier stage with a sensitivity of 5×10^{11} or 1×10^{11} V/C depending on the feedback capacitor, an op-amp stage with a 20x gain, and a unity gain buffer amplifier. The buffer amplifier stage has a bandpass filter formed from a high-pass filter and a low-pass filter with cutoff frequencies of 23 Hz and 21 kHz, respectively. The high-pass filter in front of the buffer amplifier eliminates any DC bias from the second stage, whereas the low-pass filter reduces high frequency noise.

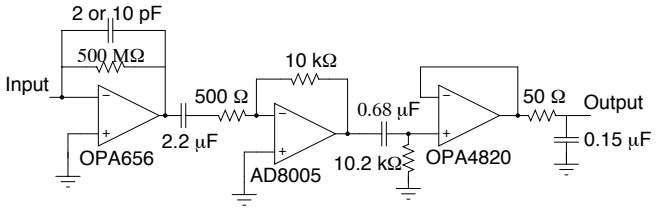

FIG. 3. The electronic schematic of the charge sensitive amplifiers used in the ablation chamber. The first and second stage have a combined sensitivity of 1×10^{13} or 2×10^{12} V/C (depending on the feedback capacitor used), and the third stage is a unity gain buffer amplifier with a bandpass filter with cutoff frequencies 23 Hz and 21 kHz.

The CSA circuits were carefully characterized and have an equivalent noise level of about 3×10^3 e^- rms. The CSA circuit is on a printed circuit board with the copper electrode on the opposite side of the board and a via connecting the electrode to the CSA input. There is a grounded plane separating the circuitry layer of the board from the electrode. Also, there is a thin (0.9 mm) grounded strip on the edge of each board's electrode that mitigates crosstalk between two adjacent electrodes/CSAs such that it is negligible. To reduce noise pickup, there is a cylindrical shield surrounding the plates (see component labled shielding in Figure 2), which also acts as a large ground bus.

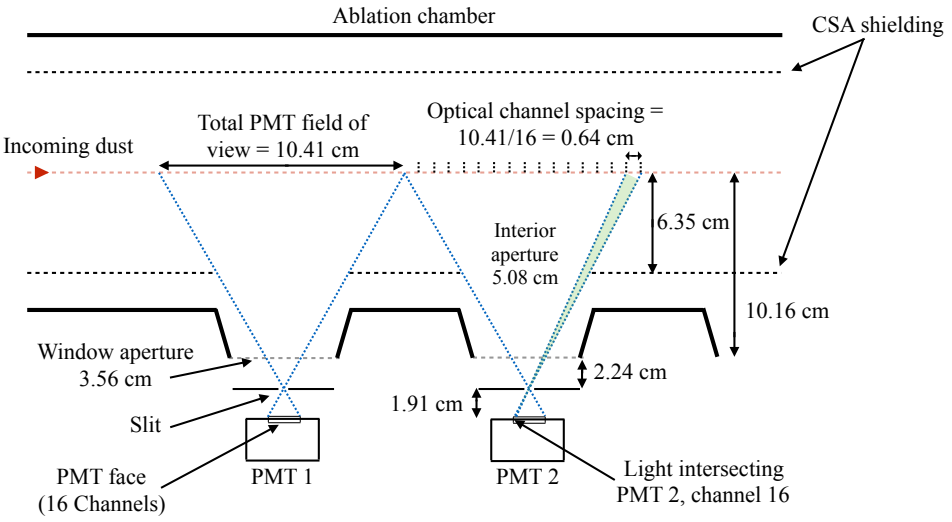

FIG. 4. Schematic of the ablation chamber PMT setup (top view). Each PMT has 16 channels with each channel having an effective area of 0.12 cm^2. The PMT has a slit between it and the window, which creates a pinhole image of the beamline on the PMT face. Since the PMT face has 16 channels spread across it, this creates 16 spatial bins along the beamline axis (0.64 cm resolution). The green region shows the view of the beamline through the slit for PMT 2, channel 1.

E. Optical Setup

Measuring the light emission from an ablating particle is useful for a number of reasons: (1) real meteors are often observed through optical measurements[30] and using two techniques simultaneously (such as radar and optical measurements) is more effective at constraining the properties of the meteors[31], and (2) one of the goals of this facility is to follow the particle's position as it moves through the ablation chamber to obtain velocity/deceleration measurements. The ability to measure the particle's velocity as it ablates allows for low-velocity β measurements (when the particle might be slowing down) and it allows for the validation of ablation model predictions. In this article, the optical data is not being analyzed in detail, but rather what follows is a description of the optical setup and preliminary velocity measurements (see Section IV B) that show this is possible.

The four windows on the ablation chamber (see Figure 2) allow for the measurement of the light produced by the ablation. A PMT setup was tested on the chamber, consisting of four Hamamatsu R5900U-16-L20 16-channel PMTs. Each channel on the PMTs has a rectangular effective area with dimensions of 0.076 x 1.6 cm (0.12 cm^2). The rectangular channels were oriented such that the larger dimension was vertical with respect to the dust trajectory. The advantage of this setup is that by placing a vertical slit in front of the PMT, it is possible to segment the ablation path into 64 distinct bins (16 bins per window) at a cost of reduced light. The slit and PMT act as a pinhole imager, so that a reversed image of the beamline falls onto the PMT face. Since the PMT face is divided into 16 channels, this segments the beamline into 16 separate spatial bins. This segmentation gives a spatial resolution of 0.64 cm along the beamline for each PMT channel.

Figure 4 shows a schematic of the ablation chamber PMT setup from a top-down perspective with only two out of the four window/PMT assemblies shown (charge collection plates not shown). There are 5.08 cm apertures cut out of the inner CSA shielding, which ensures the shielding will not obstruct the view of the beamline, and the PMTs are offset from the window to achieve the spatial binning. Figure 4 also shows the slit and the view of one of the PMT channels (green region). Specifically, the view of PMT 2, channel 16 is projected through the slit and onto the beamline axis with a 0.64 cm resolution.

With a real slit of finite width, there is a small error introduced in the assumed position of the particle. The light from a point source particle along the beamline axis going through a real slit produces a spreading, δs, on the PMT face given by

$$\delta s = w\frac{H}{h}, \tag{2}$$

where w is the slit width (0.17 cm), H is the distance from the beamline to the PMT (14.3 cm), and h is the distance from the beamline to the slit (12.4 cm). This error must be accounted for when imaging the particle.

Each PMT channel is amplified by a transimpedance amplifier, shown in Figure 5. The amplifiers have a time constant of 90 ns, which is equivalent to the transit time across a bin of a 71 km/s particle. Therefore, the PMT signals are fast enough to clearly capture a transiting particle entering and exiting a channel's field of view. Furthermore, the amplification is sufficient to observe single photon events.

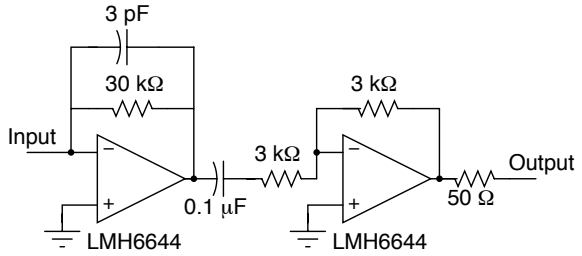

FIG. 5. The electronic schematic of the transimpedance amplifer circuit, which amplifies each PMT channel.

F. Data Acquisition

The data acquisition system used in the experiment is a multichannel system which saves all charge, impact, and light signals simultaneously with a timestamp that can be compared to the particle data that the accelerator facility produces (see Shu *et al.*[2] for a full description of the capabilities of the accelerator facility). For example, every particle shot by the accelerator is measured by the particle selection unit (PSU), which outputs a mass and velocity and is saved with a timestamp. This mass and velocity data is critical to all experiments which use the accelerator, as it provides the parameters for each particle that enters the experiment. The dust ablation facility matches (using timpestamps) its dataset with the particle parameters from the accelerator, so that each ablation event is associated with a known particle mass and velocity.

Figure 6 shows a block diagram of the data acquisition system, and the details are as follows. This setup allows for 47 channels saved for each ablation event: 16 charge signals, 1 impact signal, 1 beamline image charge detector signal, and 29 light signals. Currently the system is not capable of saving all 64 light signals, but this will be addressed in future iterations of the data acquisition. When collecting light signals, one must choose which signals to save and which to discard. For the examples shown in this article, every other PMT signal was saved (futher details are described in Section IV B). The beamline detector signal assists with matching each ablation event to the correct particle from the accelerator's measurements. A Computer-Aided Measurement and Control (CAMAC) crate is used as the data bus (LeCroy 1434 CAMAC crate), and the electronic signals are digitized by three Jorger Model TR analog digitizer cards (16 channels per card with one dead channel on one of the cards, 40 MHz, 12 bits). The data is sent over a LeCroy 8901A GPIB interface to a LabVIEW-controlled computer, where it is saved as a comma separated value (csv) file.

The Joerger cards are triggered by a carefully timed digital pulse from the PSU. As a particle moves down the beamline, the PSU detects the particle and measures its parameters, as stated previously. After it has measured the particle's velocity, it then waits the correct amount of time for the particle to reach the last beamline detector. Once it does, the PSU sends a pulse to the Joerger cards and triggers them. Due to the timing restrictions of the various signals, each ablation event must be saved with the maximum sampling frequency (40 MHz) and contain $\sim$ 20,000 data points per channel. Therefore, each ablation event contains $\sim$ 1.4 MB of raw data, and with a GPIB interface maximum data transfer rate of 450 KB/s, this produces a download time of several seconds for each ablation event. Faster, more modern, CAMAC interfaces are being investigated to reduce download time in the future.

III. MODELING

There are two types of supporting models used in the data analysis of this experiment: (1) a Monte Carlo code which calculates the collection efficiency of ions, and (2) a second Monte Carlo code which calculates any electron impact ionization enhancement as a function of pressure. Both modeling efforts are important to interpreting the experimental data from this facility and utilizing the data to validate commonly used ablation models. This section describes each of the models.

A. Collection Efficiency

In order for the ablation chamber and its diagnostics to be useful as a scientific instrument, it is important to characterize the behavior of the generated ions/electrons in the presence of the electric field. To this end, Monte Carlo simulation codes were developed to investigate the motion of the ions in the electric field and to determine the extent to which the ions spread in the chamber (the electron spread is much less due to the five orders of magnitude smaller mass). This section describes the model and presents model results.

The collisions between the ablated atoms and the molecules of the background gas are most easily described in the center-of-mass (COM) system. Since the ablated atoms leave the surface with a thermal speed (e.g. 855 m/s for a 1900 K Fe atom) that is much smaller than the velocity of the parent dust particle (typically $>$ 10 km/s), we assume that the ablated atom moves with the same velocity in the same direction as the parent particle. Similarly, we can neglect the thermal speed of molecules of the ambient gas (e.g. 476 m/s for N_2 at 300 K) and thus assume it is initially at rest in the lab frame. Let $v_{r,0}$ be the relative velocity before the collision, which equals the speed of the dust particle at the time of ablation (based on the assumptions above). The velocities of the ablated atom with mass m and the gas molecule with mass M, respectively, in the COM frame are then $v_0 = v_{r,0}(\frac{M}{m+M})$ and $V_0 = v_{r,0}(\frac{m}{m+M})$. The energy conservation before and after the collision can be written in the COM frame as

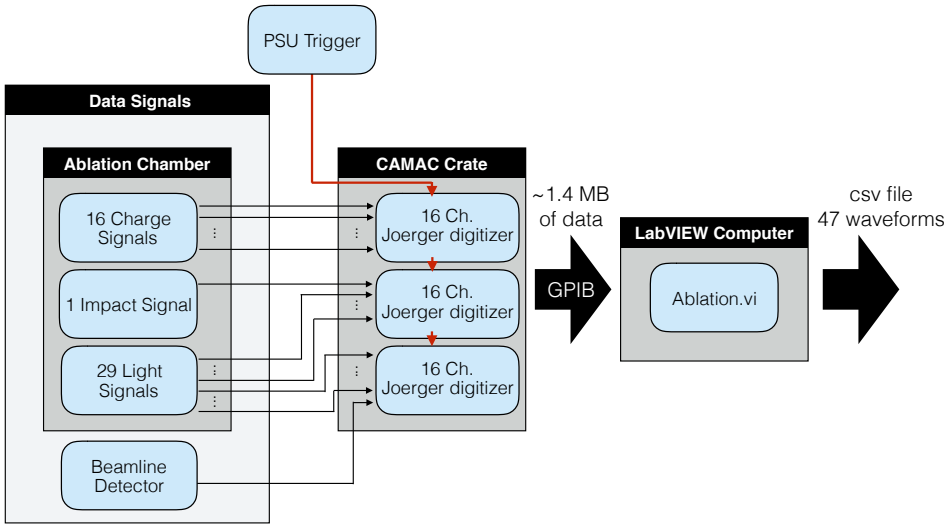

FIG. 6. A block diagram of the data acquisition system. The ablation chamber electronic signals, along with the last beamline image charge detector, are saved by three Joerger Model TR analog digitizers. The digitizers are triggered by the accelerator PSU, and the data is sent to a LabView-controlled computer. The computer saves all signals into a single file with 47 waveforms.

$$\frac{1}{2}\mu v_{r,0}^2 = \frac{1}{2}\mu v_{r,1}^2 + \Delta W, \tag{3}$$

where $\mu = mM/(m+M)$ is the reduced mass, $v_{r,1}$ is the relative speed after the collision, and $\Delta W > 0$ is the energy absorbed in inelastic collisions. For elastic collisions, $\Delta W = 0$ and $v_{r,0} = v_{r,1}$. Now let us assume that ionization occurs in the collision, thus ΔW equals the ionization potential j_{IP} and thus the relative speed after the collision is

$$v_{r,1}^2 = v_{r,0}^2 - \frac{2j_{IP}}{\mu}. \tag{4}$$

The minimum initial speed needed for ionization is calculated for the condition $v_{r,1} = 0$ and thus the minimum corresponding dust particle velocity is

$$v_{D,min}^2 = \frac{2j_{IP}}{\mu}. \tag{5}$$

The ionization potentials of 7.87 eV for Fe atoms and 15.58 eV for N_2 molecules yields 9.0 km/s and 12.7 km/s minimum dust speed, respectively. It is clear that at low velocities, the ionization of Fe atoms will dominate over N_2.

A collisional Monte Carlo code is developed after Robertson and Sternovsky [32] that follows the particles from the ionizing collision and produces a spatial distribution of the generated ions when collected on one of the electrodes. The following simplifying assumptions are made in the calculations. (1) Since the size of the dust particle (e.g. 50 nm) is much smaller than the mean free path between collisions (e.g. 143 μm at 0.5 Torr), presence of the dust particle is neglected on all subsequent processes. (2) The ionization occurs in the first collision and all subsequent collisions are elastic. (3) Hard sphere collisions with velocity-independent radii $r_{Fe} = 1.4 \times 10^{-10}$ m[33], and $r_{N_2} = 1.58 \times 10^{-10}$ m[34] are assumed. In each collision, the relative speed of the ion is randomly reoriented and in between collisions the ion is accelerated by the electric field (see Robertson and Sternovsky [32]). (4) The collision partner is selected randomly from a Maxwell-Botzmann distribution.

Figure 7 shows the spatial distribution of collected ions. Location x = 0 refers to the location where the atom is ablated from the particle, and the results show an offset distribution that is relatively symmetric. This can be explained in that the initial velocity of the particle is in the positive x-direction (going with the dust particle), and after the first collision the velocity is randomly distributed. The bias between the plates was fixed at 100 V for these simulations, the velocities investigated were 10, 20 and 40 km/s and the pressure was varied between 0.02 - 0.5 Torr, which corresponds to collision mean free paths on the order of 0.22 - 5.5 mm. The distributions resemble a Gaussian distribution for all cases investigated. The average distance traveled along the dust's path before collection is decreasing with increasing pressure and shows only a weak variation with velocity. The average value of x is typically 2 - 4 times the collision mean free path. The simulations show that for pressures $\geq$ 0.2 Torr, the ions from each ablating atom will typically be collected by the plate directly beneath the ablation event, while at the lowest pressures, the ions are likely to be collected on the next plate. The standard deviations in the x and z directions are similar and roughly equal to the average of x.

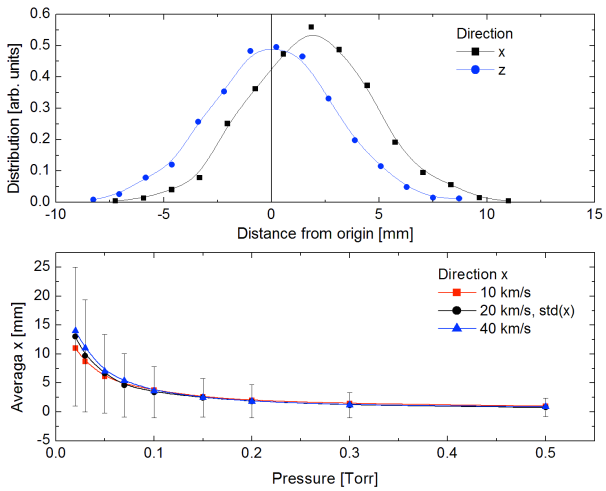

FIG. 7. The results from the Monte Carlo simulations. Top: The spatial distribution of ions collected on the electrodes for v_{dust}= 20 km/s and p = 0.2 Torr. The position x = 0 marks the place where the atom ablated from the particle. Bottom: The average position of collection (along the path of the dust particle, i.e. x-direction) as a function of pressure for three different dust velocities. The standard deviation is shown for the 20 km/s case.

This model gives the displacement (x_0) and the standard deviation (σ) of a Gaussian function given by

$$f(x|x_0,\sigma) = \frac{1}{\sigma\sqrt{2\pi}} e^{-\frac{(x-x_0)^2}{2\sigma^2}}. \quad (6)$$

The Gaussian parameters from the Monte Carlo simulation are shown in Table I, so that given any pressure and velocity, one can interpolate correct x_0 and σ values. For the instrument geometry described in section II C, we can conclude that the applied bias voltage is sufficient to collect all ions on the plates. Even for the lowest pressure and highest velocity investigated, the collection efficiency is about 95%. In future studies, the Gaussian (Equation 6) will be convolved with simulated ablation profiles, which has the effect of spreading the ions to better match experimental conditions. However, this paper is simply meant to detail the capabilities of the facility and therefore does not include ablation model results.

B. Electron Impact Ionization Enhancement

The other supporting model is also a Monte Carlo simulation used to investigate secondary ionization effects and its contribution to the total collected charge. The bias voltage applied between the collecting plates is on the order of 100 V. This means that free electrons generated in between the plates may gain sufficient energy to produce additional ion-electron pairs. These generated secondary charges would contribute to the total collected

	Displacement (x_0,mm)			
Pressure (Torr)	10 km/s	20 km/s	40 km/s	σ(mm)
0.0200	11.0	13.0	14.0	12.0
0.0300	8.70	9.70	11.0	9.70
0.0500	6.10	6.60	7.00	6.80
0.0700	4.83	4.60	5.36	5.50
0.100	3.75	3.39	3.62	4.40
0.150	2.57	2.45	2.48	3.33
0.200	1.97	1.83	1.81	2.84
0.300	1.43	1.14	1.19	2.17
0.500	0.98	0.77	0.85	1.59

TABLE I. Monte Carlo results of ion spreading in the ablation chamber run at 100 V bias between the top and bottom ablation plates. The displacement is the center value of the Gaussian, while σ is the standard deviation.

charge and inflate the β measurements (β measurements described in detail in Section IV A).

The simulation effort described below follows the motion of electrons accelerated towards the positive collection plates and collisions with the background gas are modeled in a Monte Carlo fashion. The calculations presented are for N_2, since that is the most relevant constituent of Earth's atmosphere. In the simulations, the electrons start with zero kinetic energy half way in between the biased collector plates. The accelerating electric field is $E = U/d$, where U is the potential applied across the collecting plates separted by $d = 3.6$ cm. The accelerated electrons undergo collisions with a total cross section of

$$\sigma_{TOT} = \sigma_{ion} + \sigma_{excit} + \sigma_{elast} \quad (7)$$

where σ_{ion} is the ionization cross section, σ_{excit} is the excitation cross section, and σ_{elast} is the elastic cross section. Figure 8 shows the cross section model derived from Phelps and Pitchford [35], however, simplifications are made because of the large number of ongoing processes. The elastic (or momentum transfer cross section) is the largest with a strong resonant feature at around 2 eV electron energy. One possible channel for the inelastic collisions is the rotational excitation of the molecules, in which the electrons only loose a relatively small amount of energy (0.02 eV). Electrons can loose between 0.29 and 2.35 eV over a range of possible vibrational excitation collisions[35]. For simplicity, the model assumes that the weighted average of 1 eV is lost in each collision and the cross sections are summed up over all possibilities. There are multiple channels for electron excitation collisions as well. These collisions were separated into two categories (number 1 and 2 in Figure 8) with an average energy loss of 8 and 12 eV, respectively. Electrons gaining energy larger than 15.6 eV are capable of ionizing the nitrogen molecules with a cross section increasing with increasing electron energy. The model assumes that each collision results in a random isotropic reorientation of the primary electrons' velocities.

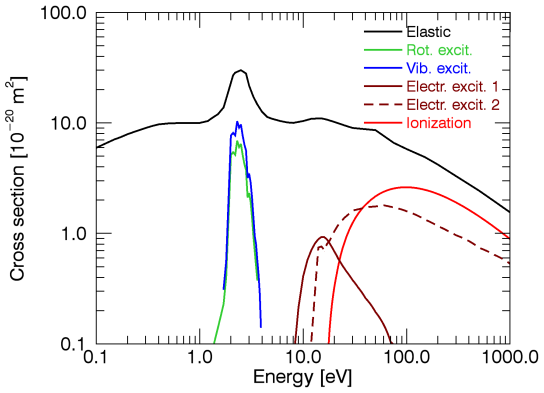

FIG. 8. The cross sections of the various types of N_2-e^- collisions included in the secondary ionzation model. Currently the model only includes N_2 gas. See text for more details.

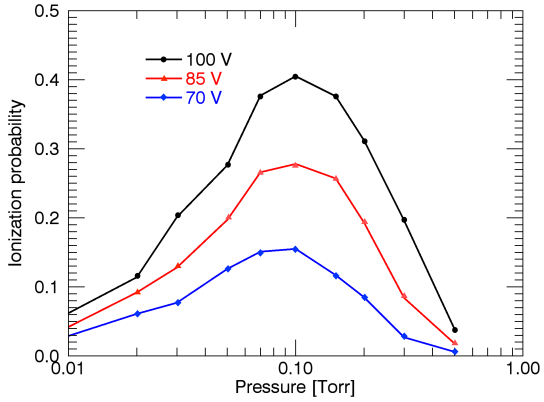

FIG. 9. The probability (as a function of pressure and bias voltage) that a free electron, generated directly by the ablation process, will generate an additional ion-electron pair before it is collected. The calculations are for N_2 and a gap distance of d=3.6 cm.

Figure 9 shows the results of the numerical model, which is the probability that an electron starting in the middle of the ablation chamber will produce an additional ion-electron pair on its way towards the collecting electrode. This probability depends on both the bias voltage applied across the electrodes, as well as the pressure of the background gas. For the parameters investigated, the maximum occurs at a pressure of about 0.1 Torr, which corresponds to a pressure-gap length of pd = 0.36 Torr·cm. This value is comparable to the position of the minimum in the breakdown voltage on the Paschen curve[36], suggesting that the mechanism for the maximum is similar. For example, the ionization probability decreases for lower pressures because there are fewer collisions between electrons and neutrals and decreases for larger pressures because electrons do not gain sufficient energy in between collisions for ionization to occur. The more detailed analysis of the collision processes reveals that electron excitation collisions play an effective role in limiting the attainable electron energy and thus reducing the probability of ionization. The roughly 40% ionization probability for the investigated parameter range also means that the cascading breakdown of the gas can be neglected. This is not surprising, given that the maximum applied bias voltage is much below the Paschen discharge voltage ($>$ 300 V[36]).

We next apply the results of this model to the ionization coefficient values that were recently reported in Thomas *et al.*[1]. Figure 10 shows the reported β values for iron impacting N_2. Other gases have not yet been added to the model, and so the following discussion is limited to N_2 only. The β values are labeled by the ablation chamber pressure and the bias voltage used, and each data set has an estimated percentage of additional ionization. The bias voltages were between 70-90 V and were used in conjuction with the pressure to determine the percentage. It is not obvious from Figure 10 that there is any pressure dependence to β, and this was in fact the justification given in Thomas *et al.*[1] to neglect the possibility of additional ionization in that analysis.

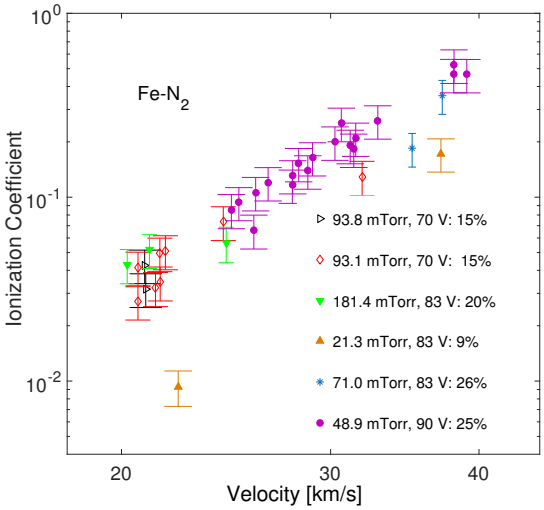

FIG. 10. The ionization coefficient (β) vs. velocity for iron particles impacting N_2, which was recently reported in Thomas *et al.*[1]. The β values are color coded by ablation chamber pressure with the bias voltage and estimated additional ionization precentage labeled.

Due to the bias voltages used in that experiment, the effect was relatively mitigated except perhaps for the 71 and 48.9 mTorr data. The error bars on each data point are $\sim$ 22%, which would place those β values slightly outside of the reported error bars. The effect will be mitigated in future studies by using a bias voltage of 70 V, unless the pressure used in the experiment is sufficiently low or high for the effect to be negligible.

IV. EXPERIMENTAL DATA

Examples of experimental data are shown below in order to demonstrate the capabilities of the facility. Charge

and light measurements with spatial resolution, a first for laboratory experiments, are shown along with a basic analysis which calculates β and measures the velocity of an ablating particle. It is demonstrated that the spatial resolution of the charge measurements, along with the velocity measurements, will allow for experimental validation of ablation models in future studies.

A. Charge Measurements

Figure 11 shows an example of the charge data (ions) collected by the experiment. In this example, the iron particle had a velocity of 45.6 km/s and the ablation chamber was pressurized with air to 15 mTorr. The CSAs have a much longer time constant than the time it takes to collect the charges, and so the CSAs integrate the charge that each electrode collects. Therefore, the peak of each signal gives the total charge collected by that electrode. Five peaks are labeled in Figure 11 (channels 4-8) that show the gradual increase and decrease of ionization as the particle travels down the ablation chamber.

Figure 12 shows the total number of ions collected on each channel (i.e. the peak voltage on each channel converted to charge). The ionization coefficient is the ratio of elementary charges produced to the total number of atoms ablated. Therefore, for an ablation event where the particle completely ablates (such as this example), the ionization coefficient can be calculated as $\beta = N_{ions}/N_{Fe}$, where N_{ions} is the total number of ions/electrons collected across all channels (3.5 million for this particle) and N_{Fe} is the total number of atoms in the dust particle (8.5 million). For this particle, β was found to be 0.41. This procedure was done for a variety of target gases (N_2, air, CO_2, and He) and across a wide range of velocities (20-90 km/s). The results of that study have been presented by Thomas *et al.*[1].

One important distinction between this facility and previous experimental ablation facilities (see for example Friichtenicht, Slattery, and Hansen[21] and Slattery and Friichtenicht[20]), is that this facility has 16 charge collection plates. The plates give spatially-resolved measurements over the entire ablation profile, and this allows for the comparison between experimental ablation profiles and the predicted profiles from ablation models. The purpose of this article, however, is to simply demonstrate the experimental capabilities of the facility. Comparisons between experimental ablation profiles, like that found in Figure 12, to those predicted by ablation models will be done in future studies.

B. Light Measurements

An example of an ablation event with both the charge and the PMT signals is shown in Figure 13. The PMT channels are arranged chronologically from top to bottom, and in this example, the channels are separated by

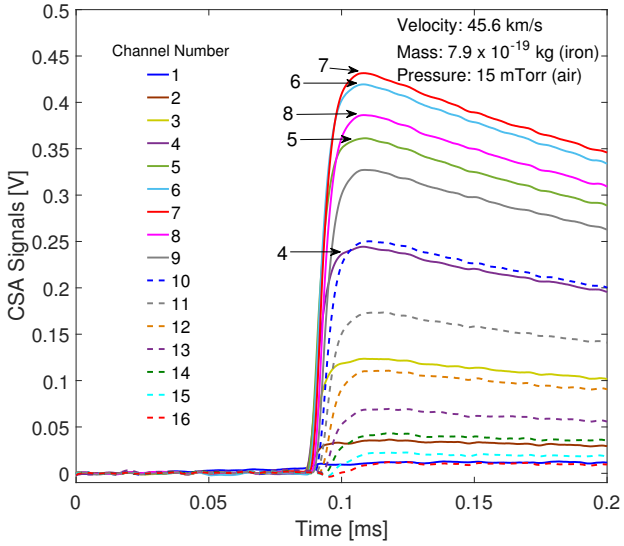

FIG. 11. An example of a particle ablating in the experimental chamber. The figure shows the charge collection CSA signals vs. time. In this case, the experiment was configured to collect ions.

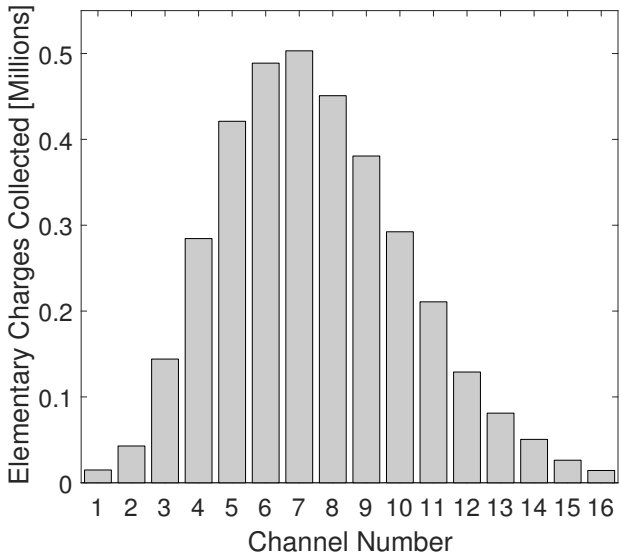

FIG. 12. Ions collected by each electrode channel for the particle ablation event shown in Figure 11. The 16 segmented collectors give a spatial resolution of 2.6 cm for the charge measurements, which will allow for comparisons to ablation model predictions in future studies.

0.64 cm (i.e. every other PMT channel was collected) and channels prior to the first light signal are not shown. Specifically, due to the limited light channels the data acquisition is able to record with the current setup (29), the light signals which were saved for the event in Figure 13 were arranged in the following way. The first channel was saved, followed by the third, fifth, etc. all the way to channel 55. Channel 56 was also saved such that the total was 29. For this event, the PMTs detected mostly

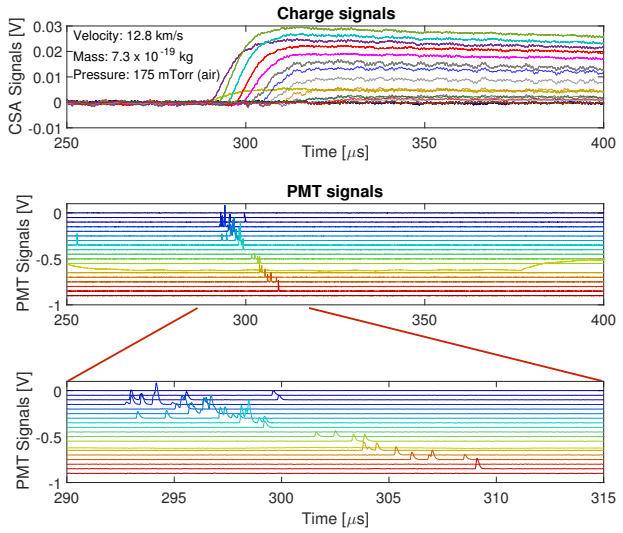

FIG. 13. An example ablation event with both the charge and PMT signals shown. The charge signals are color coded to match Figure 11. The PMT channels are artificially offset from one another, with the channels organized in chronological order from top to bottom.

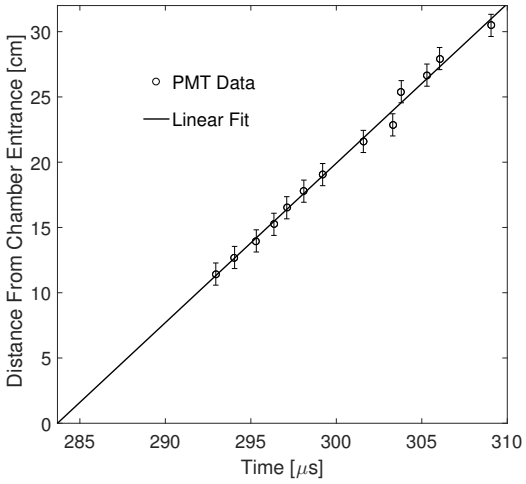

FIG. 14. The PMT pulse times from Figure 13 plotted as distance from the chamber entrance vs. time. The data was fit to a linear fit, which gives an average velocity of 12.21±0.29 km/s compared to a beamline measured velocity of 12.77±0.38 km/s.

single photon events, which is due to a combination of the light production efficiency and the geometry of the PMT setup. The transimpedance amplifiers are capable of amplifying single photon events well above the noise (as is evident in Figure 13).

In order to measure the dust velocity from the PMT signals, the times for the start of each pulse were measured and are shown in Figure 14. Care must be taken when selecting PMT pulses for Figure 14. Each PMT channel may have multiple pulses and it is possible a pulse may be caused by background photons or PMT dark current, rather than from a direct viewing of the particle itself. Furthermore, there is a position error on each data point that is a combination of PMT pulse rise time ($\sim$ 100 ns), the size of the PMT bins (0.64 cm), and the slit width error (δs, see Equation 2). The calculation of the total error is as follows. First, the PMT pulse rise time error was converted to a position error based on the particle velocity (provided from the acclerator). Next, the sum of the PMT bin size error and δs was added in quadrature to the PMT pulse rise time error to obtain a total error for each data point (±0.85 cm). These are the vertical error bars shown in Figure 14.

After carefully selecting PMT pulses, a least-squares linear fit was made to the data (black line in Figure 14) which gave a velocity of 12.21±0.29 km/s, compared to 12.77±0.38 km/s measured from the beamline detectors. The total error on the fit was found by first calculating the root mean squared error (rmse). The rmse is given by[37]

$$\sigma_y = \sqrt{\frac{1}{N-2}\sum_{i=1}^{N}(y_i - A - Bx_i)^2}, \tag{8}$$

where σ_y is the rmse on the linear function $y = A + Bx$, N is the number of data points in the fit (13), and A and B are the best estimates of the coefficients. The error on the slope (i.e. velocity) is then[37]

$$\sigma_B = \sigma_y\sqrt{\frac{N}{\Delta}}, \tag{9}$$

where $\Delta = N\sum x^2 - (\sum x)^2$.

The novelty of these light measurements is that it is now possible to track the dust particle as it moves through a laboratory ablation chamber. Meteor ablation models calculate the particle's velocity as it ablates, and the dust velocity measurements described here will provide the necessary experimental data to verify those calculations. However, as stated previously, the purpose of this work is to simply demonstrate the capability. The ablation model analysis will be done in future studies.

V. SUMMARY

We present a new experimental facility for simulating micrometeroid ablation in the laboratory. The facility includes an ablation chamber and a differential pumping system which attaches to the end of the IMPACT dust accelerator at the University of Colorado. The accelerator is capable of producing dust particles from 1-100 km/s with radii of 20 nm - 5μm.

The ablation chamber contains a suite of electronics which collect the generated plasma from an ablated dust particle over two sets of 16 segmented collectors. The collectors allow for a spatial resolution of 2.6 cm and allow for the comparison between experimental ablation profiles and profiles generated by ablation models. The charge measurements also allow for β measurements for a variety of dust and gas types (see Thomas *et al.*[1] for the first β results of the facility).

In addition to charge measurements, the ablation facility is configured to enable the measurement of light production as a particle ablates. The chamber has four windows evenly spaced along the ablation path that allow for the placement of PMTs to measure the dust velocity as it ablates. Future experiments will use dust velocity and charge generation measurements to constrain ablation models.

VI. ACKNOWLEDGMENTS

This research is supported by NASA SSERVI at the Institute for Modeling Plasma, Atmospheres, and Cosmic Dust (IMPACT) and also NASA grant NNX15AJ96G. J.M.C. Plane is funded by the European Research Council, Project 291332 - CODITA.

VII. REFERENCES

[1]E. Thomas, M. Horányi, D. Janches, T. Munsat, J. Simolka, and Z. Sternovsky, Geophys. Res. Lett. **43**, 3645 (2016).
[2]A. Shu, A. Collette, K. Drake, E. Grün, M. Horányi, S. Kempf, A. Mocker, T. Munsat, P. Northway, R. Srama, Z. Sternovsky, and E. Thomas, Review of Scientific Instruments **83**, 1 (2012).
[3]W. Jones, Monthly Notices of the Royal Astronomical Society **288**, 995 (1997).
[4]J. M. C. Plane, Chemical Society Reviews **41**, 6507 (2012).
[5]D. Nesvorný, P. Jenniskens, H. F. Levison, W. F. Bottke, D. Vokrouhlický, and M. Gounelle, ApJ **713**, 816 (2010).
[6]D. Nesvorný, D. Janches, D. Vokrouhlický, P. Pokorný, W. F. Bottke, and P. Jenniskens, ApJ **743**, 1 (2011).
[7]J. M. C. Plane, Chemical Reviews **115**, 4497 (2015).
[8]Z. Ceplecha, J. Borovicka, W. G. Elford, D. O. Revelle, P. V. Hawkes, R. L., and M. Simek, Space Sci Rev **84**, 327 (1998).
[9]W. J. Baggaley, in *Meteors in the Earth's Atmosphere*, edited by E. Murad and I. Williams (Cambridge University Press, 2002) pp. 123–148.
[10]A. Pellinen-Wannberg and G. Wannberg, J. Geophys. Res. **99**, 11379 (1994).
[11]S. Close, R. Volz, R. Loveland, A. Macdonell, P. Colestock, I. Linscott, and M. Oppenheim, Icarus **221**, 300 (2012).
[12]D. Janches, L. P. Dyrud, S. L. Broadley, and J. M. C. Plane, Geophysical Research Letters **36**, 1 (2009).
[13]L. Dyrud and D. Janches, Journal of Atmospheric and Solar-Terrestrial Physics **70**, 1621 (2008).
[14]D. Janches, M. C. Nolan, D. D. Meisel, and J. D. Mathew, Journal of Geophysical Research **108**, 1 (2003), 1222.
[15]D. Janches, J. M. C. Plane, D. Nesvorny, W. Feng, D. Vokrouhlicky, and M. J. Nicholls, The Astrophysical Journal **796**, 1 (2014b).
[16]D. L. Bones, J. C. Gómez Martín, C. J. Empson, J. D. Carrillo Sánchez, A. D. James, T. P. Conroy, and J. M. C. Plane, Rev. of Sci. Instrum. **87**, 1 (2016).
[17]Y. F. Bydin and A. M. Bukhteev, Soviet Physics-Technical Physics **5**, 512 (1960).
[18]A. Moutinho, A. Baede, and J. Los, **51**, 432 (1971).
[19]J. F. Cuderman, Phys. Rev. A **5**, 1687 (1972).
[20]J. C. Slattery and J. F. Friichtenicht, The Astrophical Journal **147**, 235 (1967).
[21]J. F. Friichtenicht, J. C. Slattery, and D. O. Hansen, Phys. Rev. **163**, 75 (1967).
[22]J. F. Friichtenicht and D. G. Becker, The Astrophysical Journal **166**, 717 (1971).
[23]T. Vondrak, J. M. C. Plane, S. Broadley, and D. Janches, Atmos. chem. Phys. **8**, 7015 (2008).
[24]E. Thomas, S. Auer, K. Drake, M. Horányi, T. Munsat, and A. Shu, Planetary and Space Science **89**, 71 (2013).
[25]J. L. Chau, R. F. Woodman, and F. Galindo, Icarus **188**, 162 (2007).
[26]L. Hood and M. Horányi, Icarus **93.2**, 259 (1991).
[27]O. Kalashnikova, M. Horányi, G. E. Thomas, and O. B. Toon, Geophysical Research Letters **27**, 3293 (2000).
[28]S. Auer, in *Interplanetary Dust*, edited by E. Grün, B. A. S. Gustafson, S. F. Dermott, and H. Fechtig (Heidelberg: Springer, 2001) pp. 383–444.
[29]A. Collette, E. Grün, D. Malaspina, and Z. Sternovsky, Journal of Geophysical Research: Space Physics **119.8**, 6019 (2014).
[30]M. D. Campbell-Brown, Earth, Moon, and Planets **95**, 521 (2005).
[31]R. G. Michell, D. Janches, M. Samara, J. L. Hormaechea, C. Bruini, and I. Bibbo, Planetary and space Science **118**, 95 (2015).
[32]S. Robertson and Z. Sternovsky, Phys. Rev. E. **67**, 1 (2003).
[33]J. C. Slater, Journal of Chemical Physics **40**, 3199 (1964).
[34]Cleveland, Ohio, 56th ed. (1975).
[35]A. V. Phelps and L. C. Pitchford, Phys. Rev. A **31**, 2932 (1985).
[36]V. A. Lisovskiy, S. D. Yakovin, and V. D. Yegorenkov, J. Phys. D: Appl. Phys. **33**, 2722 (2000).
[37]J. R. Taylor, *An Introduction to Error Analysis*, 2nd ed. (University Science Books, 1997) pp. 186–188.